Rapid Thermally Processed Hierarchical Titania-based Hollow Fibres with Tunable Physicochemical and Photocatalytic Properties

Tianlong Zhang,[1] Muthia Elma,[2,3] Fengwei Xie,[1,4,5] Julius Motuzas,[2] Xiwang Zhang,[6] David K. Wang[2,7]*

[1] School of Chemical Engineering, The University of Queensland, Brisbane, Queensland 4072, Australia.

[2] The University of Queensland, FIM^{2}Lab – Functional Interfacial Materials and Membranes Laboratory, School of Chemical Engineering, The University of Queensland, Brisbane Qld 4072, Australia.

[3] Lambung Mangkurat University, Chemical Engineering Department, Jl. A. Yani KM 36 Banjarbaru, South Kalimantan, 70714, Indonesia.

[4] Institute of Advanced Study, University of Warwick, Coventry CV4 7HS, United Kingdom

[5] International Institute for Nanocomposites Manufacturing (IINM), WMG, University of Warwick, Coventry CV4 7AL, United Kingdom

[6] Monash University, Department of Chemical Engineering, Faculty of Engineering, Clayton, Victoria 3800, Australia

[7] The University of Sydney, School of Chemical and Biomolecular Engineering, New South Wales 2006, Australia. *Correspondence author email: david.wang1@sydney.edu.au

Abstract

A series of photocatalytic TiO_2–carbon composite hollow fibres (HFs) was prepared in this study by a wet-dry phase inversion spinning method followed by a rapid thermal processing (RTP). The RTP method consists of two stages: (1) calcination at 800 °C for 15 min encased in a quartz tube followed by (2) a short open heating exposure at 800 °C for 0 to 7.5 min in air. The innovative two-stage RTP method led to a time saving of more than 90%. Results revealed that the pyrolysis conditions during the second stage of HF fabrication were essential to the final physical and chemical properties of resultant TiO_2-carbon HFs, such as TiO_2 crystallinity and carbon content, mechanical, textural and electronic properties, as well as photocatalytic reactivity. The best results show that HFs pyrolysed for a short duration (< 2 min) in the second stage produced a high microporous surface area of 217.8 $m^2 \cdot g^{-1}$, a good mechanical strength of 11 MPa and a TiO_2 anatase-to-rutile (*A/R*) ratio of 1.534 on the HF surface. The HFs also achieved a 68% degradation of acid orange 7 dye with a k_{app} of 0.0147 min^{-1} based on a Langmuir-Hinshelwood model during the photocatalysis under UV light. Thus, this work provides a new synthesis protocol with significant time and cost savings to produce high-quality HFs for wastewater treatment.

Keywords: Hollow fibre; Titanium dioxide; Rapid thermal processing; Photocatalysis; Carbon char

1. Introduction

A tremendous, concerted research effort in designing advanced, integrated technologies for wastewater treatment and water purification while reducing energy and environmental footprint has gained momentum. Pollution arising from the wastewater effluents of the dye

industry leads to the destruction of ecosystems and to the detriment of human health. Without adequate and proper treatment of these dye-containing effluents to remove the harmful toxic dyes before discharge, these effluents can cause short-term acute ecotoxicity and long-term bioaccumulation in ecosystems.

In the last decade, photocatalytic membranes in various geometry and size have been reported [1, 2]. There are several technological and environmental challenges relating to the use of photocatalytic nanomaterials for water treatment. Titanium dioxide, or titania (TiO_2), an n-type transition metal oxide semiconductor, has been widely utilised as a photocatalyst to initiate the degradation of organic pollutants. It has been applied to photocatalytic oxidation of several industrial and pharmaceutical effluents, such as 4-methoxybenzyl alcohol [3], ciprofloxacin [4], reactive dyes [5, 6], nitrobenzene [7, 8] and benzylparaben [9]. When a higher photon energy than the band gap of TiO_2 (anatase 3.20 eV and rutile 3.02 eV) is absorbed, electrons will be excited from the filled valence band (VB) to the empty conduction band (CB), leaving negative electrons in the CB and positive holes in the VB. The energy of excited electron–hole pairs will either react with oxygen or water and eventually generate highly reactive hydroxyl radicals to decompose hazardous organic compounds [10, 11]. Therefore, TiO_2 nanoparticles are widely investigated as a well-known, effective and stable photocatalyst. As a photocatalyst in a slurry system, TiO_2 nanoparticles need to be reclaimed to minimise the negative environmental influence [5]. The release of TiO_2 nanoparticles to the environment will have a long-term toxicity and ecological impact on the aquatic organisms [12], even though TiO_2 is considered to be biocompatible and FDA approved as a colour additive for human use [13-15].

To satisfy these requirements, it is essential to immobilise TiO_2 nanoparticles onto a solid support while keeping the TiO_2 exposed on the surface for maximising photocatalysis efficacy. It is well documented that sol-gel syntheses using TiO_2 precursors, including tetrabutyl

orthotitanate [16], titanium isopropoxide [17, 18], titanium tetrachloride [19], and titanium glycolate [20], followed by dip-coating [21] and a calcination process can be used to construct the photocatalytic devices for environmental applications. However, the conventional thermal calcination is time-intensive and requires a high-temperature sintering process to coalesce the inorganic oxides together to confer desired properties such as mechanical strength and photoactivity. Despite this, TiO_2 is known to undergo grain growth and usually a phase transformation from the anatase to rutile phases during the high-temperature thermal process at 400–600 °C for powders [22] or at 700–800 °C for non-powders [2, 23-25]. Such changes will significantly decrease the photocatalysis efficiency for the intended purposes. Therefore, a new protocol is urgently needed to avoid not only the energy penalty but also the undesired morphological changes.

Thus, in this paper, an innovative two-stage rapid thermal processing (RTP) protocol is developed for the synthesis of TiO_2-supported hollow fibres (HFs). This technology was firstly applied in the preparation of glass-carbon HFs by sintering particle-polymer-solvent systems to pyrolyse the polymer [26]. As the HF configuration has an extremely high surface area to volume ratio and a sponge-like, porous inner structure [27], TiO_2-carbon HFs can create a reactor that has an increasing selectivity and efficiency by combining photocatalysis and phase separation processes in one step [15, 28, 29]. The new RTP protocol takes the advantage of partially carbonizing the polymer binder with a very short heating duration (in minutes) under a constant temperature of 800 °C.

Essentially, RTP involves a simple, short, rapid firing/dwell time during the calcination process to significantly reduce the fabrication time. As RTP is an emerging technique for fabricating inorganic thin film membranes, the main principle of RTP is to heat the top layer with a short isothermal hold before rapidly cooling the HFs to room temperature. This method allows only the top layer to be heat-treated to achieve the desired structure/properties whilst

keeping the support relatively intact. The first stage involves a short partial pyrolysis of the polymer binder to form composite of TiO_2–carbon HFs, which is then subjected to a second stage RTP protocol to create the hierarchical porous TiO_2–carbon HFs, where the TiO_2 is surface-exposed for photocatalysis whilst the carbonaceous char offers mechanical strength and microporosity as a structural support. In addition, the presence of carbonaceous material has previously been demonstrated to reduce TiO_2 aggregation and the phase transformation during high-temperature calcination [30, 31]. Therefore, this study systematically investigates the effect of RTP (fast and short temperature-heating protocol) on the mechano-physicochemical and photocatalytic properties of the final composite HFs for the decomposition of organic pollutants in wastewater.

2. Experimental

2.1 Chemicals and materials

In this study, all the chemicals and reagents were from Sigma Aldrich (ACS grade) and used without further purification. The specific details of the Degussa P25 titanium dioxide (TiO_2) nanoparticles were reported in an earlier study [32].

2.2 Fabrication of HF membranes

To prepare the HFs, a spinning-pyrolysis technique was employed [2]. Briefly, Degussa P25 TiO_2 powder was mixed with poly(ether imide) (PEI) and 1-methyl-2-pyrrolidinone (NMP) as a solvent at an 18:25:75 ratio (w/w) for 24 h until a homogenous state was achieved, and then degassed under vacuum for another 24 h. The spinning dope was then extruded through a tube-in-orifice spinneret (OD = 2.5 mm and ID = 0.8 mm). The pressure in the spinning dope and airgap was maintained at 4 bars and 50 mm, respectively. Phase inversion was induced from the inner side of the HFs using deionised (DI) water as a bore fluid followed by the outside in a DI water bath, where the green fibres were left immersed for 24 h. Then,

the TiO_2/PEI green fibres were dried for 24 h at 60 °C. A muffle furnace was used for the calcination without the introduction of any specialised gases, which was preheated to 800 °C. Before pyrolysis, the green fibres were placed inside a double open-ended quartz tube (length = 20 cm; OD = 8 mm) to minimise the geometric curvature. In the first-stage calcination, the HFs were directly placed into the preheated furnace for a fixed 15 min holding time followed by cooling for 15 min outside of the furnace until reaching room temperature. Then in the second-stage RTP calcination, the HFs were removed from the quartz tube and calcined again in a preheated furnace (800 °C) for a pre-determined time of 0 to 7.5 min. During the two-stage RTP treatment, PEI was pyrolysed into carbonaceous char to afford the final composite TiO_2–char HFs.

2.3 Characterization techniques

The morphological structure of the pyrolysed composite HFs was examined using a field-emission scanning electron microscope (FESEM JEOL 7001F operating at 10 kV). The crystal structure and phase composition of the HFs (after grinding) were analysed by a powder X-ray diffraction system (XRD, Bruker AXS D8 advance, Cu-Ka radiation). Nitrogen sorption measurement of the HFs was performed using Micromeritic TriStar 3000 instrument after degassing the samples at 200 °C overnight under vacuum on a VacPrep061 (Particle and Surface Sciences Pty). The specific surface area was determined using the Brunauer, Emmett and Teller (BET) method and the total pore volume was taken from the last point of the adsorption isotherm (*ca.* 0.94 P/P_o). The cumulative pore volume distribution was determined from the adsorption branch of isotherms using the Density Functional Theory (DFT) model of cylindrical pores with oxide surfaces. Dubinin-Astakhov and Barrett-Joyner-Halenda methods were taken to determine the average pore diameter of microporous and mesoporous materials, respectively. A three-point bending test was performed using an Instron 5543 universal machine with a set strain rate of 1 $mm \cdot min^{-1}$ to measure the mechanical strength of the

composite HFs. The maximum bending strength was calculated using the following expression for a simple tube adapted from previous studies [33, 34]:

$$\sigma = \frac{8FLD}{\pi(D^4 - d^4)} \quad (1)$$

where σ is the bending strength (MPa), F is the load applied (N), and L, D and d are the span, the outer diameter and the inner diameter (mm) of the HFs, respectively. The UV-visible diffuse reflectance spectra of the HFs were recorded by a UV-Vis spectrophotometer (Evolution 220, Thermo Scientific) from 185 to 700 nm.

2.4 Photocatalysis evaluation of the HFs

The photocatalytic activity of the composite HFs was evaluated using four UV-A lamps (SYLVANIA Blacklite F8W/BL350, 330-370 nm emission; 8 Watt each) as the UV source. Acid Orange 7 (AO7) was used as a model colour dye due to its excellent stability under UV irradiation [35]. 25 mL of AO7 (5 ppm; pH 6.5) in a quartz reactor vessel was placed concentrically at 15 cm away from the UV lamps in the UV chamber to minimise the heating effect of the UV lamps. HF membranes weighing about 50 mg (4 × 1 cm pieces; membrane surface area: approximately 1.5×10^{-4} m^2) were submerged in the AO7 solution in the reactor. Scheme 1 shows the batch catalytic reactor containing HFs and AO7 solution.

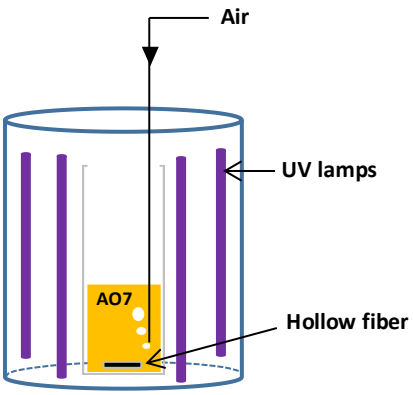

Scheme. 1. Reactor set-up for AO7 photocatalysis.

A 30-min dark sorption experiment was performed prior to switching on the UV lamps. During the photocatalysis under UV exposure, the temperature of the reactor was gradually increased from room temperature (22 °C under air condition) to about 40 ± 1 °C, of which the impact on the photodegradation of the AO7 dye was considered insignificant based on our observation, and hence, the effect was neglected in this study [2, 36]. The UV-Vis spectrum of the feed solution was recorded from 220 nm to 620 nm by a UV-Vis spectrophotometer (Evolution 220, ThermoScientific). The concentration of AO7 was determined by measuring the absorbance at 485 nm based on an established standard calibration curve. The photocatalytic activity of the membrane can be determined by the percent degradation of AO7 in the feed solution based on the equation,

$$\text{AO7 degradation (\%)} = (C_0 - C_t)/C_0 \times 100\% \qquad (2)$$

where C_0 and C_t are the AO7 concentration in the reactor solution before photocatalysis (after dark sorption) and at a reaction time t, respectively. The UV absorbance of the AO7 solution was measured every 15 min until the experiment was stopped at 75 min.

3. Results and Discussion

3.1 HF morphology and properties

In the first stage, partial pyrolysis of HFs was carried out in an encased quartz tube to minimise direct heat transfer that would otherwise decompose the polymer binder completely. Instead, the HFs were pyrolysed for 15 min under this condition without any need of speciality gases and formed a homogeneous composite of TiO_2-char HFs. As shown by the digital micrographs in Fig. 1, all the HFs had an average outer diameter and an inner diameter of 1.40 ± 0.10 mm and 0.67 ± 0.07 mm, respectively. When the HF was only exposed to the first-stage calcination (0 min), the appearance of the HFs was completely black, which is attributed to the characteristic colour of the carbonaceous char. After this stage, the 0-min HF lost 27% of its original mass as a result of the pyrolysis. As the time of the second-stage RTP calcination was extended from 1 to 7.5 min, the HFs (without the quartz sleeves) were exposed to the high temperature in an oxidative environment, which resulted in a systematic loss of the char as the black colour diminished from the outside inward progressively. As shown in Table S1, the HF mass also decreased rapidly to the minimum of 42 wt% due to the decomposition of the char.

Unsurprisingly, the white colour attributed to the TiO_2 nanoparticles emerged as the char was decomposed. It is interesting to note that the second-stage RTP heat treatment was predominately governed by the surface heat transfer from the outside to the inside of the HFs instead of a homogeneous heat treatment. This is a hallmark feature of the RTP technique which undertakes the adiabatic heating process [37]. As a result of this, with low calcination times (< 2 min), the HFs possessed a TiO_2-exposed surface whilst keeping the bulk of the HFs a composite architecture at its inner luminal core. From this treatment protocol, one can appreciate that RTP is generally a surface treatment confined to the top layer of a thin film to reach the desired temperature with the char support experiencing only a mild temperature gradient [37, 38].

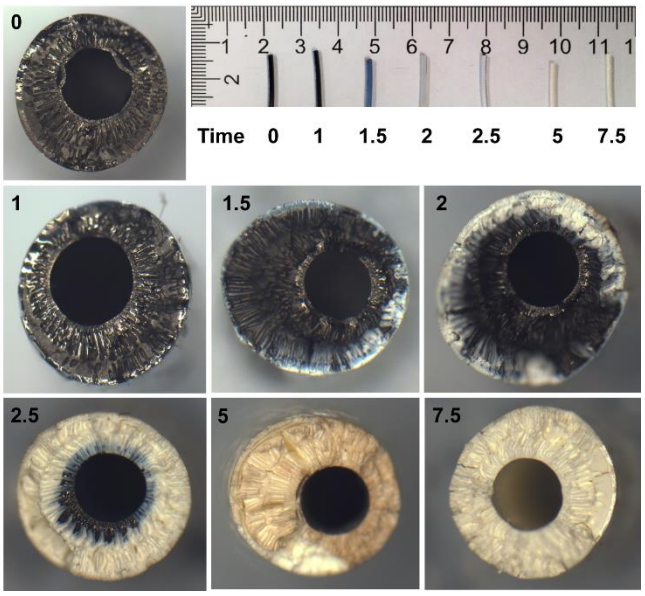

Fig. 1. Light microscopic images of TiO_2–char composite HFs with increasing RTP calcination time (0-7.5 min) at 800 °C.

Further visual examination of the HFs was carried out by SEM. Fig. 2 shows the cross-sectional SEM images of the 1, 2 and 7.5-min HFs at the outer edge near the surface. With a short calcination time, the 1-min HF displayed a large quantity of PEI-derived char matrix, which bound TiO_2 nanoparticles. For the 2-min sample, the carbonaceous matrix was seen to be partially removed at the outer edge and TiO_2 nanoparticles were partially exposed. This SEM observation is in agreement with the light microscopic images. Further RTP treatment (7.5 min) removed all the carbonaceous char in the HFs and only the regular TiO_2 nanoparticles with approximately 50 nm in size remained after the calcination.

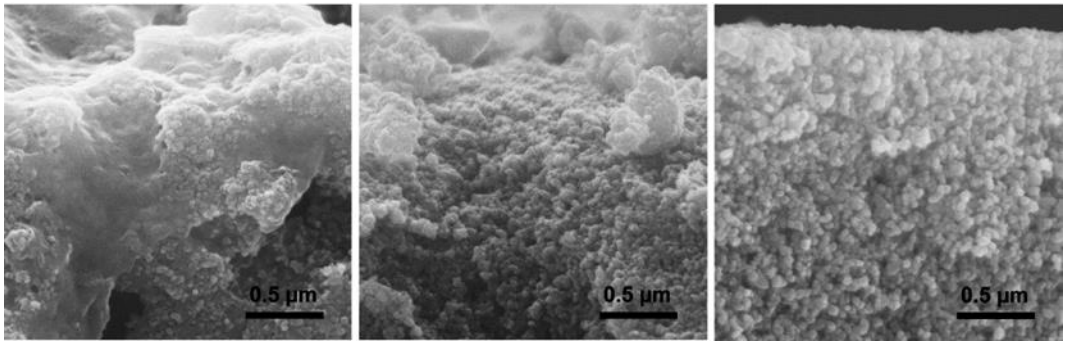

Fig. 2. Cross-sectional SEM images of composite TiO_2-char HFs treated for different RTP calcination times (1, 2 and 7.5 min, left to right).

The textual property changes of the calcined HFs during RTP processing were supported by the N_2 physisorption data. Fig. 3(a) shows the N_2 physisorption isotherms while Fig. 3(b) displays the results of surface area and average pore diameter of the HFs as a function of RTP calcination time (0-7.5 min). From Fig. 3(a), at 0 min, the HF possessed a highly microporous texture as shown by a rapid increase in N_2 adsorption at a relatively low partial pressure of 0.2 P/P_o and without any hysteresis at 0.9 P/P_o. As the RTP time increased, the microporous portion derived from the char decreased sharply from 1 min to 7.5 min as depicted by the loss in surface area in Fig. 3(b). Concurrently, the average pore size of the HFs increased as the char was decomposed leaving only the voids between TiO_2 nanoparticles, which is in good agreement with the SEM images. This can also be inferred from the increasing pore diameter of the HFs from 2.7 to 26.4 nm as the RTP time increased, which demonstrates a systematic enlargement of the mesopores in the bulk. Based on the microscopic examination and the physisorption results, these mesopores are therefore found to be located mostly at the outer part of the HFs but as the RTP time increased, the mesopores and macropores completely ensued the entirety of the HFs due to the removal of microporous char. Moreover, it can be concluded that the textual property of the HFs was hierarchical and asymmetric with shorter RTP times (< 2 min). From the N_2 adsorption/desorption isotherms and pore size distribution, hierarchical macro-

meso-microporous characteristics were shown in these HFs samples in the cross-sectional, radial direction along the fibre axis, which might indeed enhance the mass transport in chemical reactions due to the increased surface area, and thus improve its overall catalytic efficiency [39, 40].

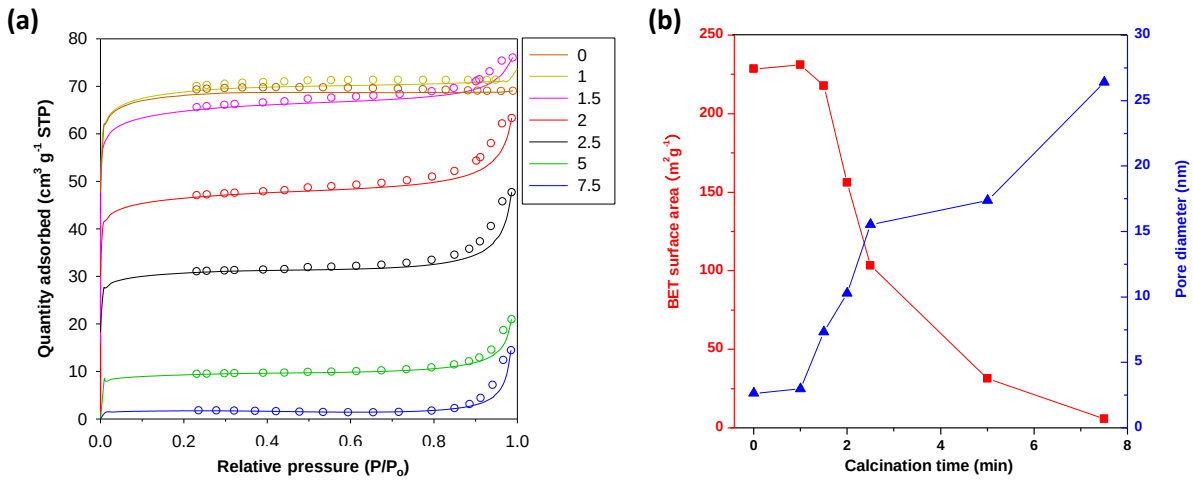

Fig. 3. (a) Nitrogen adsorption (line) and desorption (open circles) of the composite HFs and (b) BET surface area and average pore diameter as a function of RTP time (0-7.5 min).

The mechanical property of the composite HFs in terms of fracture strength was also examined by three-point bending tests. In previous studies, it was found that the carbonaceous matrix in silica composites can significantly enhance the mechanical strength due to an increased structural integrity formed by carbon-silica interconnection [41, 42]. Also, high mechanical properties have been demonstrated in metal-carbon nanotubes composites [43]. Similarly, the maximum bending stress results in Fig. 4 show that the removal of the carbonaceous matrix led to a reduction in flexure stress. With increasing RTP calcination time from 0 to 7.5 min, the maximum bending stress declined dramatically from 61 MPa to 2 MPa. Moreover, the bending stress of the 2-min sample reduced to half those of the 1-min and 1.5-

min samples. Therefore, it is necessary to use a short RTP time to maintain superior mechanical properties since the carbonaceous matrix acts as an important physical support to the overall HFs.

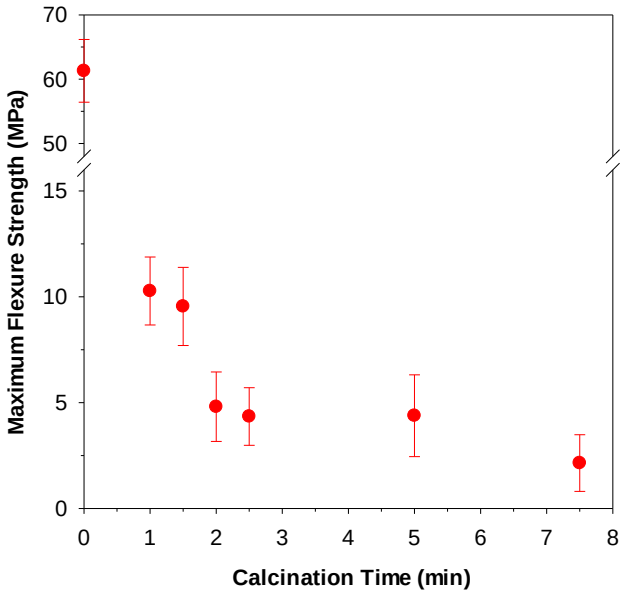

Fig. 4. Mean of maximum bending stress (MPa) plus two standard deviations of the composite HFs as a function of RTP calcination time.

The crystal morphology and phase composition of the TiO_2 photocatalyst are also significant factors directly affecting the photocatalytic property of the HFs. Fig. 5(a) displays the XRD results of the TiO_2 crystallinity on the HF surface with respect to RTP time. The 0-min sample showed mixed anatase and rutile phases as indicated by highly intense XRD peaks at 25.4° 2θ (1 0 1) and 27.4° 2θ (1 1 0), respectively. These peaks in the spectra match the JCPDS files 89-4921 and 89-4202 of tetragonal systems for the pure anatase phase and the pure rutile phase, respectively [44]. A clear trend can be seen that the disappearance of the anatase phase was offset by the emergence of the rutile phase. In general, TiO_2 turns into the anatase

phase by calcination between 300 °C and 400 °C and transforms into the rutile phase when the temperature reaches above 600 °C [45]. However, this change was not found in this current study where the RTP temperature was set at 800 °C, which is significantly above this phase transition temperature. Regarding this, we propose that the TiO_2 nanoparticles were thermally shielded by a sacrificial layer of carbonaceous matrix. Hence, the anatase phase of TiO_2 was still predominantly preserved in the 0 to 2-min samples. This fact was most evidenced by the different crystalline composition of the surface versus interior layers of the 2-min HF as shown in Fig. 5(b). As the HF surface was continuously exposed to heat, the anatase TiO_2 rapidly turned into the rutile phase yet the lumen of the HFs still possessed a high degree of anatase TiO_2.

From the XRD results, it can be seen that the transition from the anatase to rutile phase was easily controlled by the RTP time. By further analysing the anatase and rutile phase mass fractions from the intensities, the anatase-to-rutile (*A*/*R*) ratio of the HF samples can be calculated using Spurr's equation [46, 47]:

$$f_a = (\,1 + 1.26\,{}^{I_r}\!/_{I_a})^{-1} \qquad (3)$$

$$f_r = (1 - f_a) \qquad (4)$$

$${}^{A}\!/_{R}\; ratio = ({}^{f_a}\!/_{f_r}) \qquad (5)$$

where f_a and f_r are the anatase and rutile fractions and I_a and I_r are the integrated intensities of the most intense peaks of anatase (1 0 1) and rutile (1 1 0), respectively. Fig. 5 (c) shows that the *A/R* ratio on the HF surface decreased systematically from 3.13 (0 min) to 0.30 (2.5 min) and then the ratio almost became nil (0.05). The *A/R* ratio of TiO_2 crystalline morphology once

again confirms that a shorter RTP time is desirable for an optimal balance between the anatase/rutile TiO_2 phases.

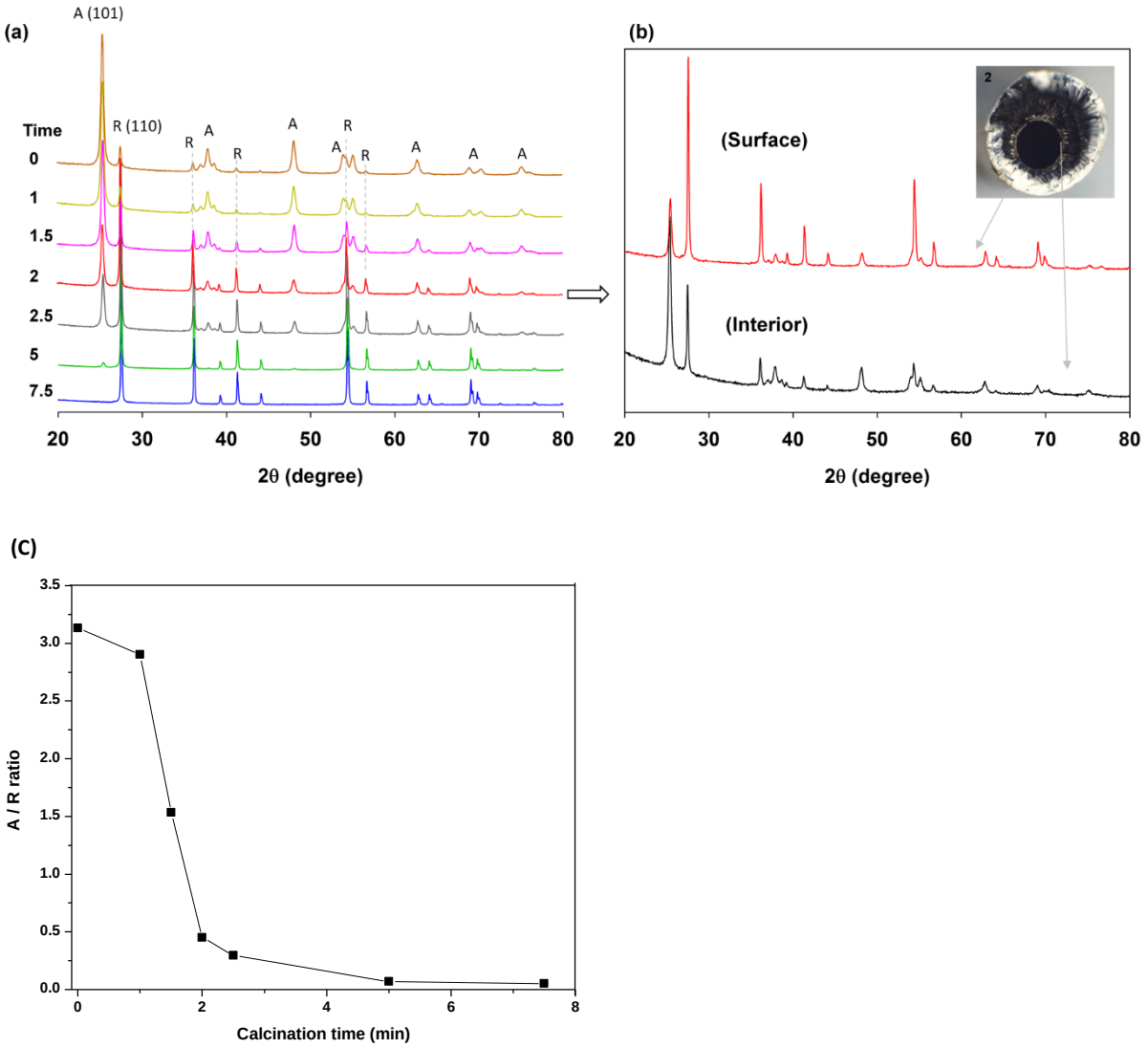

Fig. 5. (a) XRD patterns of the composite TiO_2–char HFs as a function of RTP calcination time; (b) XRD analyses of the surface and interior section of the 2-min HF sample; and (c) *A/R* ratio of the HF surface with increasing RTP time.

The effect of RTP calcination time on the optical property of grounded composite HFs was also investigated by diffuse reflectance spectroscopy. The results after baseline correction are

shown in Fig. 6. At a first glance, the absorbance scales significantly with increasing RTP time, while the spectra for the 0 and 1-min samples mostly overlap. It is well known that TiO_2 has a strong UV absorption capability as a semiconductor [22, 48, 49], while those of carbonaceous char is considered to be relatively non-UV absorbing [50, 51]. As the carbonaceous matrix enveloped the TiO_2 nanoparticles, the UV-visible light was hindered from reaching the TiO_2 surface. This was especially the case for the 0 and 1-min HFs. However, as the calcination time increased, the char matrix decomposed rapidly to expose the TiO_2 surface, whilst changing the TiO_2 phase from predominantly anatase to pure rutile. Hence, as the calcination time was extended, the surface of TiO_2 nanoparticles was increasingly exposed leading to an increasing UV absorption, which corroborates our previous characterization results.

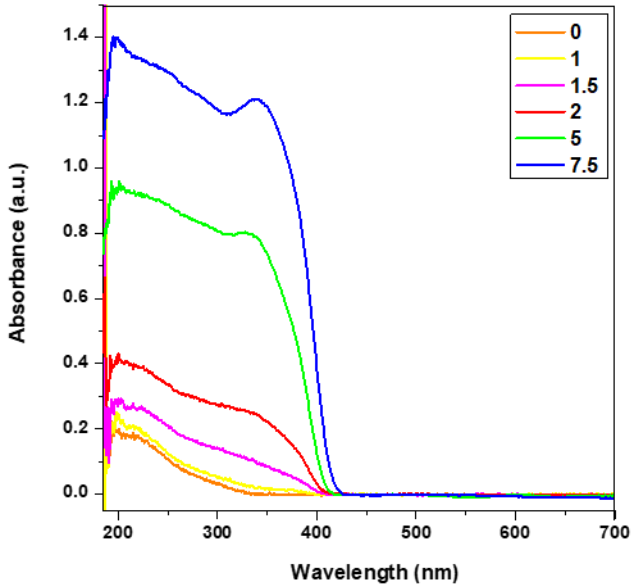

Fig. 6. Diffuse reflectance UV-vis spectra of HF samples treated for different RTP times (0-7.5 min).

3.2 Photocatalytic properties

The photocatalytic degradation of AO7 (5 ppm) dye by the HFs (50 mg) was studied by measuring the UV-Vis absorbance of the solution every 15 min up to 75 min. Prior to the experiment, 30 min of dark absorption was carried out to reach a stable AO7 concentration. No concentration change was found before and after dark adsorption showing negligible physical adsorption of AO7 on the HFs. As shown in Fig. **7**, the UV-vis spectra of the AO7 solution with the 2-min HF sample between 200 and 600 nm displayed several characteristic absorption bands of AO7 molecules. The decrease in intensity of UV bands at 485 nm (hydrazine form) and 432 nm (azo) is characteristic of the N=N azo bond cleavage because of the photocatalytic degradation of AO7 molecules [52-54]. At the same time, the intensity of peaks at 310 nm and 230 nm increased, indicating the production of small molecules with naphthalene and benzene ring, such as *p*-phenolsulfonic acid, 1,2-naphthaquinone and phenol, from the AO7 photo-degradation process [52, 55].

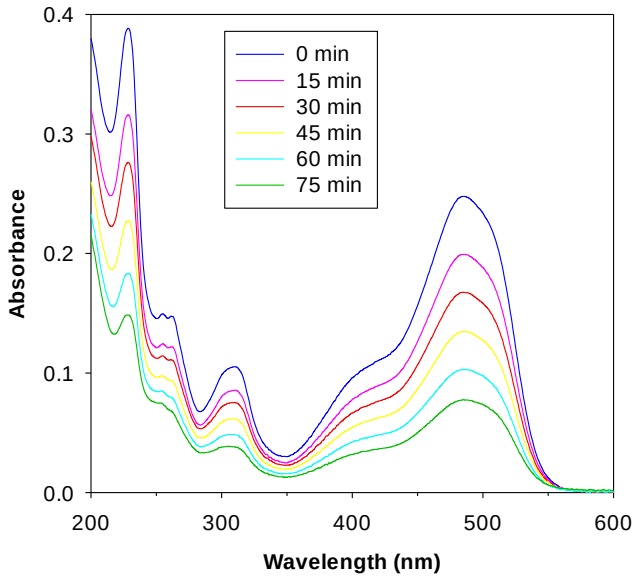

Fig. 7. Representative UV-Vis spectra during AO7 degradation process by the 2-min TiO_2–char HF sample.

Fig. 8(a) displays the AO7 photo-degradation percentage as a function of time for all the HFs under UV light with five repeated measurements. The highest AO7 removal percentage (68%) was obtained by the 1.5-min HF at the end of the photodegradation experimental period (75 min). Interestingly, it can be observed the maximum photodegradation increased first and then decreased with increasing RTP calcination time. Fig. 8(b) illustrates the AO7 degradation rate (%) produced by the HFs as determined by a logarithm equation with the AO7 initial and final concentrations (C/C_0) with respect to the photocatalysis time. In this figure, the trends of the AO7 photodegradation by different HF samples can be clearly seen whereby the 1.5-min HF again produced the fastest degradation rate.

To evaluate the photoreactivity of HF samples, the Langmuir-Hinshelwood (L-H) model has been applied to interpret the photocatalytic degradation of AO7, which is often used for the photocatalytic reaction kinetics for organic pollutants. The relationship of the degradation rate (r) and the concentration of the pollutant (C) can be expressed as below:

$$r = -\frac{dC}{dt} = \frac{k_r k_{ad}}{1+k_{ad}C} \quad (6)$$

$$\frac{1}{k_{ad}} = \frac{1}{k_r}C + \frac{1}{k_r k_{ad}} \quad (7)$$

where k_r is the intrinsic rate constant and k_{ad} is the adsorption equilibrium constant.

If adsorption is relatively weak or if the concentration of the targeting pollutant is relative low (5 ppm in this work), then two microscopic constants (k_r and k_{ad}) can be integrated as one computed constant (k_{app}), which can be used to express the reaction by a simplified form of pseudo-first order kinetics [56, 57]:

$$\ln\left(\frac{C}{C_0}\right) = -k_r k_{ad} t = -k_{app} t \qquad (8)$$

The linear fitting of ln(C/C_0) with respect to time (t) is plotted in Fig. 8(b), while the first order constant k_{app} and the coefficient of fitting, R^2, are calculated and listed in Table S2. From Fig. 8(b), k_{app} increases from 1 to 1.5 min and then gradually decreases as the RTP time increases. It is found that the 1.5-min HF offered the highest efficiency of photocatalysis with a k_{app} constant of 0.0147 min^{-1}. Although the 7.5-min sample had the greatest amount of the exposed TiO_2 photocatalyst according to the SEM results, the AO7 degradation rate only reaches a k_{app} of 0.0099 min^{-1}. This is because that all the TiO_2 anatase phase was transformed into the rutile phase which can be seen in Fig. 5(c). This result is consistent with the earlier report of the trend of photocatalytic efficiency and TiO_2 crystal morphology [10, 58].

As shown in the schematic in Fig. 9, even though the *A/R* ratio of the 1.5-min sample (1.534) is lower than the 1-min sample (2.904) on the HF surface, the former performed much better as the k_{app} value is 25% greater than the 1-min HF (0.0117 min^{-1}). This suggests that the presence of the carbonaceous matrix hindered the access of both UV light and AO7 molecules from reaching the TiO_2 nanoparticle surface. The thermal decomposition of the char matrix in the second stage exposed the photocatalyst and revealed the TiO_2 active surface, leading to an increase in photoactivity. However, by over-extending the RTP time to 7.5 min, the removal of the char matrix led to a total transformation of the TiO_2 crystalline morphology and a 35% loss of the photocatalytic efficiency. Hence, a balance of all these important properties of the HFs is critical and can be achieved by a relatively short RTP duration using the dual-stage protocol.

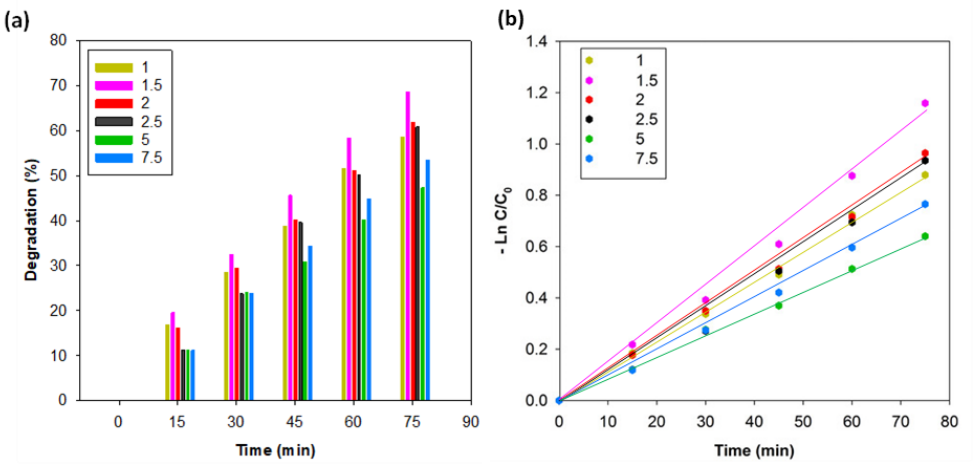

Fig. 8. Photodegradation of AO7 by TiO_2–char composite HFs under UV light irradiation: (a) using HFs with various calcination times during the second stage; (b) reaction kinetics and linear line of best fit was obtained with R^2 correlation of > 0.979.

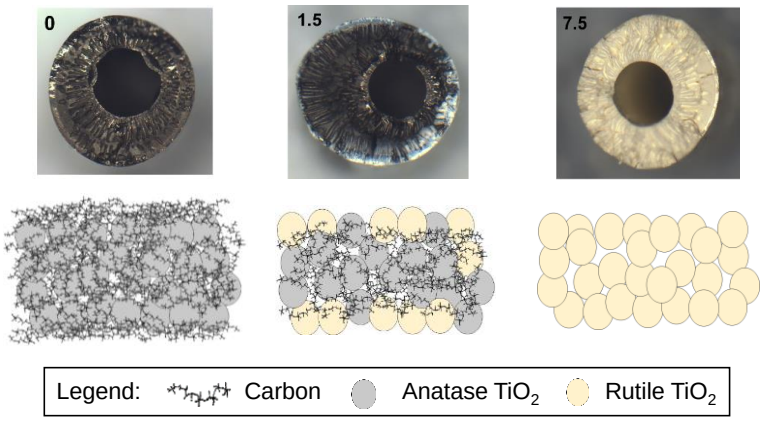

Fig. 9. Schematic representation of HFs formation by the RTP process with different second-stage calcination times.

Conclusions

In this work, an innovative, effective rapid thermal treatment method was developed to construct photocatalytic TiO_2–char composite HFs by partial pyrolysis at 800 °C in less than 30 min. The results show the mechanical strength of HFs mainly depends on the RTP pyrolysis time while the photocatalytic reactivity and efficiency are based on the *A*/*R* ratio in TiO_2 crystalline morphology as well as the degree of char decomposition of the HF surface. A promising HF sample was achieved having a reasonable mechanical strength of 11 MPa and an AO7 removal percentage of 68% with a k_{app} of 0.0147 min^{-1} for the photodegradation of AO7 under UV light. This work provides a rapid and simple calcination protocol for the thermal processing of photocatalytic composite materials and hollow fibres as well as for other interesting material geometries for wastewater treatment and environmental applications.

Acknowledgments

The authors acknowledge the facilities, the scientific and technical assistance, of the Australian Microscopy & Microanalysis Research Facility at the Centre for Microscopy and Microanalysis, The University of Queensland (UQ). D.K. Wang thanks the funding given by the University of Sydney Faculty of Engineering and Information Technology Early Career Grant, the Australian Research Council Discovery Early Career Researcher Award (DE150101687), and Sydney Southeast Asia Centre for the Workshop and Regional Mobility Grants. F. Xie acknowledges the European Union's Marie Skłodowska-Curie Actions (MSCA) and the Institute of Advanced Study (IAS), University of Warwick for the Warwick Interdisciplinary Research Leadership Programme (WIRL-COFUND).

References

[1] H. Zhang, X. Quan, S. Chen, H. Zhao, Y. Zhao, Fabrication of photocatalytic membrane and evaluation its efficiency in removal of organic pollutants from water, Separation and Purification Technology, 50 (2006) 147-155.

[2] X. Zhang, D.K. Wang, D.R.S. Lopez, J.C.D. da Costa, Fabrication of nanostructured TiO 2 hollow fiber photocatalytic membrane and application for wastewater treatment, Chemical Engineering Journal, 236 (2014) 314-322.

[3] S. Yurdakal, G. Palmisano, V. Loddo, V. Augugliaro, L. Palmisano, Nanostructured rutile TiO2 for selective photocatalytic oxidation of aromatic alcohols to aldehydes in water, Journal of the American Chemical Society, 130 (2008) 1568-1569.

[4] A. Hassani, A. Khataee, S. Karaca, M. Fathinia, Heterogeneous photocatalytic ozonation of ciprofloxacin using synthesized titanium dioxide nanoparticles on a montmorillonite support: parametric studies, mechanistic analysis and intermediates identification, RSC Advances, 6 (2016) 87569-87583.

[5] P. Jiang, D. Ren, D. He, W. Fu, J. Wang, M. Gu, An easily sedimentable and effective TiO2 photocatalyst for removal of dyes in water, Separation and Purification Technology, 122 (2014) 128-132.

[6] S. Jothivel, R. Velmurugan, K. Selvam, B. Krishnakumar, M. Swaminathan, Preparation, characterization and photocatalytic activity of acidic sulfated nano titania for the degradation of Reactive Orange 4 under UV light, Separation and Purification Technology, 77 (2011) 245-250.

[7] I. Nitoi, P. Oancea, M. Raileanu, M. Crisan, L. Constantin, I. Cristea, UV-VIS photocatalytic degradation of nitrobenzene from water using heavy metal doped titania, Journal of Industrial and Engineering Chemistry, 21 (2015) 677-682.

[8] K. Nakano, E. Obuchi, S. Takagi, R. Yamamoto, T. Tanizaki, M. Taketomi, M. Eguchi, K. Ichida, M. Suzuki, A. Hashimoto, Photocatalytic treatment of water containing dinitrophenol and city water over TiO2/SiO2, Separation and Purification Technology, 34 (2004) 67-72.

[9] Y. Lin, C. Ferronato, N. Deng, J.-M. Chovelon, Study of benzylparaben photocatalytic degradation by TiO2, Applied Catalysis B: Environmental, 104 (2011) 353-360.

[10] O. Carp, C.L. Huisman, A. Reller, Photoinduced reactivity of titanium dioxide, Progress in solid state chemistry, 32 (2004) 33-177.

[11] H. Yao, M. Fan, Y. Wang, G. Luo, W. Fei, Magnetic titanium dioxide based nanomaterials: synthesis, characteristics, and photocatalytic application in pollutant degradation, Journal of Materials Chemistry A, 3 (2015) 17511-17524.

[12] P. Westerhoff, G. Song, K. Hristovski, M.A. Kiser, Occurrence and removal of titanium at full scale wastewater treatment plants: implications for TiO 2 nanomaterials, Journal of Environmental Monitoring, 13 (2011) 1195-1203.

[13] A. Zhao, S. Zhou, Y. Wang, J. Chen, C. Ye, N. Huang, Molecular interaction of fibrinogen with thermally modified titanium dioxide nanoparticles, RSC Adv, 4 (2014) 40428-40434.

[14] S.A. Ansari, M.M. Khan, M.O. Ansari, M.H. Cho, Nitrogen-doped titanium dioxide (N-doped TiO_2) for visible light photocatalysis, New Journal of Chemistry, 40 (2016) 3000-3009.

[15] B.F.K. Kingsbury, Z. Wu, K. Li, A morphological study of ceramic hollow fibre membranes: A perspective on multifunctional catalytic membrane reactors, Catalysis Today, 156 (2010) 306-315.

[16] H. Liu, J.B. Joo, M. Dahl, L. Fu, Z. Zeng, Y. Yin, Crystallinity control of TiO 2 hollow shells through resin-protected calcination for enhanced photocatalytic activity, Energy & Environmental Science, 8 (2015) 286-296.

[17] J.S. Lee, K.H. You, C.B. Park, Highly photoactive, low bandgap TiO2 nanoparticles wrapped by graphene, Advanced Materials, 24 (2012) 1084-1088.

[18] A. Tôrres, E. Azevedo, N. Resende, M. Dezotti, A comparison between bulk and supported TiO2 photocatalysts in the degradation of formic acid, Brazilian Journal of Chemical Engineering, 24 (2007) 185-192.
[19] S.Y. Kim, T.S. Chang, D.K. Lee, C.H. Shin, Photocatalytic decomposition of methylene blue over nanosized titania particles, Journal of Industrial and Engineering Chemistry, 11 (2005) 194-201.
[20] M. Fathy, H. Hamad, A.E.H. Kashyout, Influence of calcination temperatures on the formation of anatase TiO 2 nano rods with a polyol-mediated solvothermal method, RSC Advances, 6 (2016) 7310-7316.
[21] K. Onozuka, B. Ding, Y. Tsuge, T. Naka, M. Yamazaki, S. Sugi, S. Ohno, M. Yoshikawa, S. Shiratori, Electrospinning processed nanofibrous TiO2 membranes for photovoltaic applications, Nanotechnology, 17 (2006) 1026.
[22] N. Guo, Y. Liang, S. Lan, L. Liu, J. Zhang, G. Ji, S. Gan, Microscale hierarchical three-dimensional flowerlike TiO2/PANI composite: synthesis, characterization, and its remarkable photocatalytic activity on organic dyes under UV-light and sunlight irradiation, The Journal of Physical Chemistry C, 118 (2014) 18343-18355.
[23] X. Zhang, J.H. Pan, A.J. Du, J. Ng, D.D. Sun, J.O. Leckie, Fabrication and photocatalytic activity of porous TiO2 nanowire microspheres by surfactant-mediated spray drying process, Mater. Res. Bull., 44 (2009) 1070-1076.
[24] D.K. Wang, M. Elma, J. Motuzas, W.-C. Hou, F. Xie, X. Zhang, Rational design and synthesis of molecular-sieving, photocatalytic, hollow fiber membranes for advanced water treatment applications, Journal of Membrane Science, 524 (2017) 163-173.
[25] D.K. Wang, M. Elma, J. Motuzas, W.-C. Hou, D.R. Schmeda-Lopez, T. Zhang, X. Zhang, Physicochemical and photocatalytic properties of carbonaceous char and titania composite hollow fibers for wastewater treatment, Carbon, 109 (2016) 182-191.
[26] S. Liu, G.R. Gavalas, Glass−Carbon Composite Hollow Fibers, Industrial & Engineering Chemistry Research, 43 (2004) 3137-3140.
[27] B.F.K. Kingsbury, K. Li, A morphological study of ceramic hollow fibre membranes, Journal of Membrane Science, 328 (2009) 134-140.
[28] X. Zhang, D.K. Wang, D.R.S. Lopez, J.C. Diniz da Costa, Fabrication of nanostructured TiO2 hollow fiber photocatalytic membrane and application for wastewater treatment, Chemical Engineering Journal, 236 (2014) 314-322.
[29] X. Tan, Z. Pang, Z. Gu, S. Liu, Catalytic perovskite hollow fibre membrane reactors for methane oxidative coupling, Journal of Membrane Science, 302 (2007) 109-114.
[30] D.K. Wang, M. Elma, J. Motuzas, W.C. Hou, F. Xie, X. Zhang, Rational design and synthesis of molecular-sieving, photocatalytic, hollow fiber membranes for advanced water treatment applications, Journal of Membrane Science, 524 (2017) 163-173.
[31] D.K. Wang, M. Elma, J. Motuzas, W.C. Hou, D.R. Schmeda-Lopez, T. Zhang, X. Zhang, Physicochemical and photocatalytic properties of carbonaceous char and titania composite hollow fibers for wastewater treatment, Carbon, 109 (2016) 182-191.
[32] X. Zhang, T. Zhang, J. Ng, J.H. Pan, D.D. Sun, Transformation of bromine species in TiO2 photocatalytic system, Environmental science & technology, 44 (2009) 439-444.
[33] F.P. Beer, E.R. Johnston, J. DeWolf, Mechanics of materials, Mc Graw Hill, page, (1992).
[34] S. Liu, X. Tan, K. Li, R. Hughes, Preparation and characterisation of SrCe0.95Yb0.05O2.975 hollow fibre membranes, Journal of Membrane Science, 193 (2001) 249-260.
[35] X. Zhang, D.D. Sun, G. Li, Y. Wang, Investigation of the roles of active oxygen species in photodegradation of azo dye AO7 in TiO 2 photocatalysis illuminated by microwave electrodeless lamp, Journal of Photochemistry and Photobiology A: Chemistry, 199 (2008) 311-315.

[36] X. Zhang, Y. Wang, G. Li, Effect of operating parameters on microwave assisted photocatalytic degradation of azo dye X-3B with grain TiO 2 catalyst, Journal of Molecular Catalysis A: Chemical, 237 (2005) 199-205.
[37] D.K. Wang, R. Chen, J. Motuzas, S. Smart, J.C. Diniz da Costa, Chapter 13 Rapid Thermal Processing of Microporous Silica Membranes, in: A. Basile, K. Ghasemzadeh (Eds.) Current trends and future developments on (bio-) membranes: silica membranes : preparation, modelling, application, and commercialization, Elsevier, Amsterdam, 2017.
[38] D.K. Wang, J.C. Diniz da Costa, S. Smart, Development of rapid thermal processing of tubular cobalt oxide silica membranes for gas separations, Journal of Membrane Science, 456 (2014) 192-201.
[39] Q. Tan, X. Bao, T. Song, Y. Fan, G. Shi, B. Shen, C. Liu, X. Gao, Synthesis, characterization, and catalytic properties of hydrothermally stable macro–meso–micro-porous composite materials synthesized via in situ assembly of preformed zeolite Y nanoclusters on kaolin, Journal of Catalysis, 251 (2007) 69-79.
[40] J. Liu, G. Jiang, Y. Liu, J. Di, Y. Wang, Z. Zhao, Q. Sun, C. Xu, J. Gao, A. Duan, J. Liu, Y. Wei, Y. Zhao, L. Jiang, Hierarchical Macro-meso-microporous ZSM-5 Zeolite Hollow Fibers With Highly Efficient Catalytic Cracking Capability, Scientific Reports, 4 (2014) 7276.
[41] M. Elma, D.K. Wang, C. Yacou, J.C.D. da Costa, Interlayer-free P123 carbonised template silica membranes for desalination with reduced salt concentration polarisation, Journal of Membrane Science, 475 (2015) 376-383.
[42] S. Katiyar, K. Mondal, A. Sharma, One-step sol–gel synthesis of hierarchically porous, flow-through carbon/silica monoliths, RSC Advances, 6 (2016) 12298-12310.
[43] Y. Cheng, C. Liu, H.-M. Cheng, S.P. Jiang, One-Pot Synthesis of Metal–Carbon Nanotubes Network Hybrids as Highly Efficient Catalysts for Oxygen Evolution Reaction of Water Splitting, ACS Applied Materials & Interfaces, 6 (2014) 10089-10098.
[44] C. Karunakaran, P. Anilkumar, P. Gomathisankar, Photoproduction of iodine with nanoparticulate semiconductors and insulators, Chemistry Central Journal, 5 (2011) 1.
[45] L. Hsu, R. Rujkorakarn, J. Sites, C. She, Thermally induced crystallization of amorphous-titania films, Journal of applied physics, 59 (1986) 3475-3480.
[46] D.A.H. Hanaor, I. Chironi, I. Karatchevtseva, G. Triani, C.C. Sorrell, Single and mixed phase TiO2 powders prepared by excess hydrolysis of titanium alkoxide, Advances in Applied Ceramics, 111 (2012) 149-158.
[47] R.A. Spurr, H. Myers, Quantitative Analysis of Anatase-Rutile Mixtures with an X-Ray Diffractometer, Analytical Chemistry, 29 (1957) 760-762.
[48] I.M. Szilágyi, B. Fórizs, O. Rosseler, Á. Szegedi, P. Németh, P. Király, G. Tárkányi, B. Vajna, K. Varga-Josepovits, K. László, WO3 photocatalysts: influence of structure and composition, Journal of catalysis, 294 (2012) 119-127.
[49] W. Zhao, W. Ma, C. Chen, J. Zhao, Z. Shuai, Efficient degradation of toxic organic pollutants with Ni2O3/TiO2-x B x under visible irradiation, Journal of the American Chemical Society, 126 (2004) 4782-4783.
[50] G. Daneshvar Tarigh, F. Shemirani, N.S. Maz'hari, Fabrication of a reusable magnetic multi-walled carbon nanotube-TiO2 nanocomposite by electrostatic adsorption: enhanced photodegradation of malachite green, RSC Advances, 5 (2015) 35070-35079.
[51] J. Ma, C. Wang, H. He, Enhanced photocatalytic oxidation of NO over g-C3N4-TiO2 under UV and visible light, Applied Catalysis B: Environmental, 184 (2016) 28-34.
[52] Y. Tao, M. Wei, D. Xia, A. Xu, X. Li, Polyimides as metal-free catalysts for organic dye degradation in the presence peroxymonosulfate under visible light irradiation, RSC Advances, 5 (2015) 98231-98240.

[53] L.C. Abbott, S.N. Batchelor, J.R.L. Smith, J.N. Moore, Reductive reaction mechanisms of the azo dye orange II in aqueous solution and in cellulose: from radical intermediates to products, The Journal of Physical Chemistry A, 113 (2009) 6091-6103.
[54] X. Li, Y. Chen, X. Hu, Y. Zhang, L. Hu, Desalination of dye solution utilizing PVA/PVDF hollow fiber composite membrane modified with TiO2 nanoparticles, J. Membr. Sci., 471 (2014) 118-129.
[55] W. Feng, D. Nansheng, H. Helin, Degradation mechanism of azo dye CI reactive red 2 by iron powder reduction and photooxidation in aqueous solutions, Chemosphere, 41 (2000) 1233-1238.
[56] J.C.-T. Lin, M.D.G. de Luna, G.L. Aranzamendez, M.-C. Lu, Degradations of acetaminophen via a K2S2O8-doped TiO2 photocatalyst under visible light irradiation, Chemosphere, 155 (2016) 388-394.
[57] K.V. Kumar, K. Porkodi, F. Rocha, Langmuir–Hinshelwood kinetics – A theoretical study, Catalysis Communications, 9 (2008) 82-84.
[58] S. Malato, P. Fernández-Ibáñez, M. Maldonado, J. Blanco, W. Gernjak, Decontamination and disinfection of water by solar photocatalysis: recent overview and trends, Catalysis Today, 147 (2009) 1-59.